Chapter 5. Synthesis of capped TiO_2 nanocrystals of controlled shape and their use with MEH-PPV to develop nanocomposite films for Photovoltaic applications

Thi Thuy Duong Vu [a,b], *Frej Mighri* [a,b,*], *Trong-On Do*[a,c] *Abdellah Ajji*[b,d],

[a]Department of Chemical Engineering, Laval University, Quebec, QC, G1V 0A6 Canada;

[b] Center for Applied Research on Polymers and Composites (CREPEC);

[c]Centre in Green Chemistry and Catalysis (CGCC);

[d]Department of Chemical Engineering, École Polytechnique of Montreal, C.P. 6079, Montreal, QC, H3C 3A7 Canada.

Published in *Journal of Nanoscience and Nanotechnology*, **2012**, 12(3), 2815-2824.

Abstract

This study presents the synthesis details of titanium dioxide (TiO_2) nanoparticles (NPs) of different morphologies using oleic acid (OA) and oleyl amine (OM) as capping agents. Different shapes of NPs, such as nanospheres, nanorods, and nanorhombics, were achieved. In order to develop nanocomposite thin films for photovoltaic cells, these TiO_2 NPs were carefully dispersed in 2-methoxy-5-(2'-ethylhexyloxy)-p-phenylene vinylene (MEH-PPV) matrix.

The properties of synthesized TiO_2 NPs and MEH-PPV/TiO_2 nanocomposites were characterized using transmission electron microscopy (TEM), thermogravimetric analysis (TGA), UV-Visible spectroscopy, and Photoluminescence technique. Obtained results showed promising properties for photovoltaic devices, especially solar radiation absorption properties and charge transfer at the interface of the conjugated MEH-PPV matrix and TiO_2 dispersed NPs.

Résumé

Cette étude présente les détails de synthèse des nanoparticules (NPs) de dioxyde de titane (TiO_2) avec différentes morphologies en utilisant l'acide oléique (OA) et l'oléylamine (OM) comme tensioactifs. Différentes formes des NPs, comme les nanosphères, les nanotubes et les nanorhombiques, ont été obtenues. Pour développer de films minces de nanocomposites pour les cellules photovoltaïques, ces NPs de TiO_2 ont été soigneusement dispersées dans une matrice de 2-méthoxy-5-(2'-ethylhexyloxy)-p-phenylène vinylène (MEH-PPV).

Les propriétés des NPs de TiO_2 et les nanocomposites de MEH-PPV/ TiO_2 ont été caractérisées en utilisant la microscopie électronique à transmission (TEM), l'analyse thermogravimétrique (TGA), la spectroscopie UV-Visible et la technique de photoluminescence. Les résultats obtenus ont montré des propriétés prometteuses pour les dispositifs photovoltaïques, spécialement les propriétés d'absorption de la radiation solaire et le transfert de charge à l'interface entre la matrice MEH-PPV et les NPs dispersées de TiO_2.

5.1. Introduction

As the global energy consumption increases continuously (it is expected to be double within next 50 years), a significantly larger fraction of our energy supply will need to be sourced from renewable sources in the very near future. Photovoltaic devices (PV), which convert the solar radiation into direct current electricity, were discovered since 1954 and are presently considered as one of the fastest growing renewable energy technologies.[1] Recently, polymer organic solar cells based on an interpenetrating network of electron donors and acceptors prepared using solutions of conjugated polymers have become attractive for use in inexpensive large area and low weight solar devices.[2–4] The newest generation and most two efficient polymer based solar cells are bulk heterojunction solar cells (BHSC) and dye sensitized solar cells (DSSC). Up to date, the most common conjugated polymers used as hole transporting materials in solar cells are poly (2-methoxy, 5-(2-ethyl-hexy-loxy)-p-phenyl vinylene) (MEH-PPV),[5,6] poly(3 -hexylthiophene) (P3HT),[7,8] and poly(2-methoxy-5-(3,7-dimethyloctyloxy)-1,4-phenylene- vinylene) (MDMO-PPV).[8] On the other hand, different kinds of inorganic nanocrystals, such as cadmium selenide (CdSe),[9] zinc oxide (ZnO),[10] cadmium sulphide (CdS),[11] and TiO_2,[12] are reported as charge acceptors.

Besides many attractive advantages, charge recombination of the photogenerated electro-hole pairs is the major disadvantage in the use of conjugated polymers as active layers in solar cells. Also, since the diffusion length of excitons in conjugated polymers is typically about 5−15 nm,[13,14] it could decay without any charge transfer from the polymer to the nanocrystals if the light excitation occurs far from the polymer/nanocrystals interface. To overcome this limitation, blending between conjugated polymers and nano-size crystal oxides (especially particle sizes in the range of 2–10 nm) has been recently proposed.[15] This could create a large interface between the polymer matrix and the dispersed nanoparticles, and as a result, enhances the charge transfer inside the nanocomposite.

In this study, we present a new simple route to synthesis nanocomposite materials for photovoltaic application based on a conjugated polymer (MEH-PPV) and capped TiO_2 nanoparticles. These capped NPs are reported to have easy shape-controlled and proper

band gap. They are also low cost materials, beside their original properties of chemical stability and nontoxicity. The first part of the study reports a synthesis process used to develop organic-capped TiO_2 nanoparticles with controllable shapes. Then the second part shows how these organic-capped TiO_2 are used to develop MEH-PPV/TiO_2 nanocomposites using a simple mixing technique. Optical properties, such UV-Visible and photoluminescence spectra, of the developed MEH-PPV/TiO_2 nanocomposites showed enhanced solar radiation absorption in visible wavelength and improved charge transfer between conjugated polymer MEH-PPV and TiO_2 NPs.

5.2. Experimental

5.2.1. Materials

All chemicals were used as received without further purification or distillation. Titanium (IV) butoxide (TB, 97%), oleic acid (OA, 90%), oleyl amine (OM, 70%), and 2-methoxy-5-(2'-ethylhexyloxy)-p-phenylene vinylene (MEH-PPV) (PS-3900) with the average molecular weight of 150,000-250,000 were purchased from Sigma - Aldrich Chemical, Canada. Absolute (pure) ethanol (EtOH) and 95% EtOH (with 5% water) from Brampton Canada, chloroform from Fisher Scientific Canada, and toluene from Anachemia Canada Inc., were all of analytical grade.

5.2.2. Synthesis of TiO_2 nanoparticles

The synthesis of OA-capped anatase TiO_2 nanocrystals was done at low temperature by hydrolysis of TB using OA or OM as capping agents, followed by the synthesis step reported earlier by our research group.[16] Typically, 1 mmol of TB was added to a mixture of OA and OM and absolute EtOH. The obtained mixture was stirred for 10mins then transferred into a Teflon-lined stainless steel autoclave containing absolute or 95% EtOH to keep equilibrium in the mixture in order to avoid any change in EtOH concentration during the crystallization process. The system was then heated at 150^{o}C for 18 hrs. The obtained TiO_2 nanocrystals were washed with toluene and EtOH several times then dried at room

temperature. After purification, TiO_2 was re-dispersed in chloroform or toluene solvent for characterization and composite preparation.

By keeping the amount of TB constant and varying the other parameters, such as the amount and molar ratio of OA and OM surfactants, the concentration of EtOH and the reaction temperature, different shapes of TiO_2 NPs are to be achieved.

5.2.3. Synthesis of MEH-PPV/TiO_2 nanocomposites

MEH-PPV polymer and TiO_2 NPs of known MEH-PPV/TiO_2 ratios were first dissolved into $CHCl_3$ then mixed together for 24 hrs at room temperature. In order to improve the dispersion of TiO_2 NPs into the MEH-PPV matrix, low frequency ultrasound sonication was applied for 2 mins before any characterization of the MEH-PPV/TiO_2 nanocomposite.

5.2.4. Characterization

Size and morphology characterization of TiO_2 NPs were done at 120 kV using a JEOL JEM 1230 transmission electron microscope (TEM). Samples were prepared by dispersing TiO_2 NPs in toluene solvents in a first step; then one drop of the mixture was placed onto a 200 mesh carbon-coated copper grid and evaporated immediately at room temperature. The crystalline phases of NPs were characterized on a Bruker SMART APEXII X-ray diffractometer operated at 1200 W power (40 kV, 30 mA) to generate Cu Kα radiation (λ = 1.5418 Å). Thermal analyses of the as-synthesized TiO_2 NPs were carried out up to 650 ^oC at a heating rate of 10^oC/min under air atmosphere using a Perkin-Elmer TGA thermogravimetric analyzer. The room temperature UV-visible spectra of TiO_2 and MEH-PPV/ TiO_2 in $CHCl_3$ were recorded using a Cary 300 Bio UV-visible spectrophotometer. Pure $CHCl_3$ was used as a blank solvent. Room temperature photoluminescence (PL) spectra of MEH-PPV/ TiO_2 in $CHCl_3$ were measured on a Varian Carry Eclipse fluorescence spectrophotometer. The Fourier transform infrared absorption spectroscopy (FTIR) spectra were measured using Nicolet 380 FT-IR with a thermo

scientific smart performer ATR module and one reflection ZnSe crystal. The characterization was done at room temperature using atmosphere as background.

5.3. Results and Discussion

5.3.1. Synthesis and characterization of capped TiO_2 nanoparticles

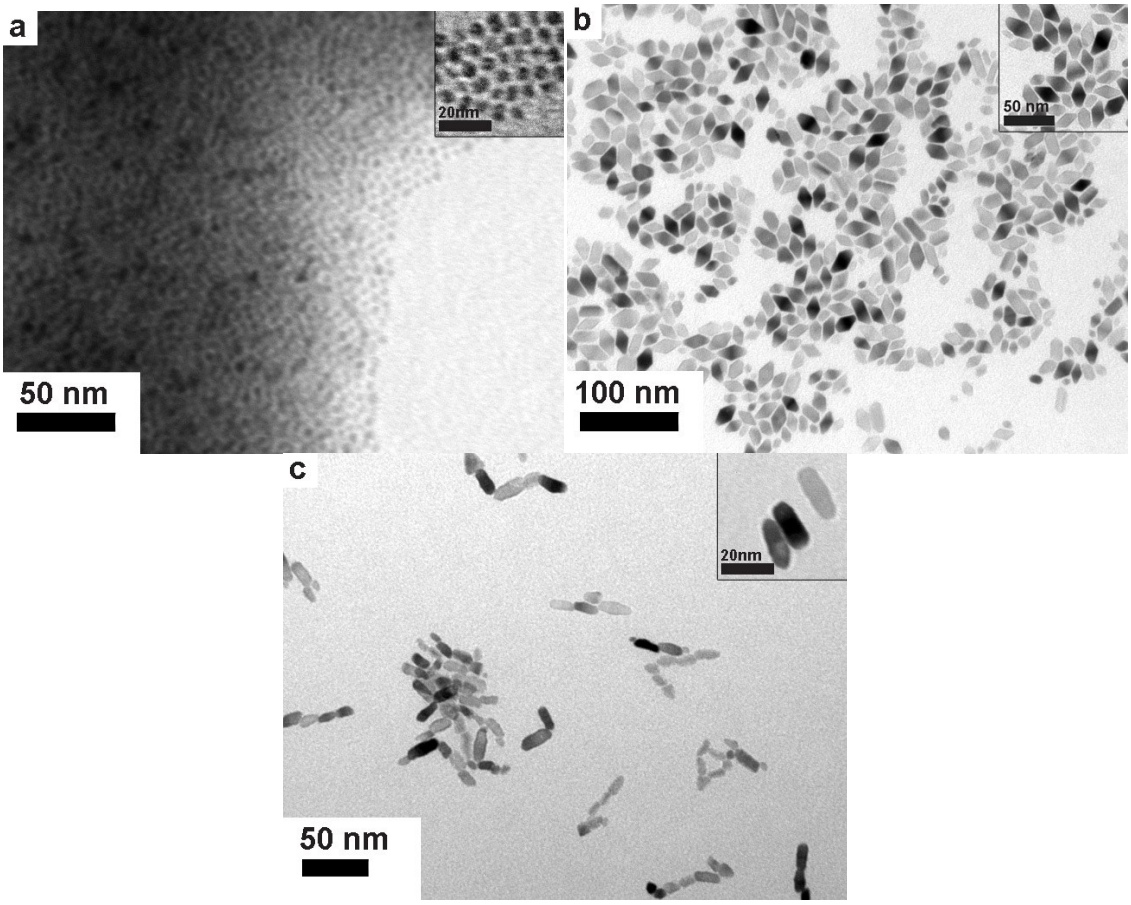

Figure 5.1. TEM of synthesized TiO_2 NPs with different shapes: (a) nanosphere, (b) nanorhombic, and (c) nanorod.

Figure 5.1 shows TEM images of TiO_2 NPs synthesized by keeping the molar ratio of TB unchanged while varying other synthesis parameters, as presented TiO_2 NPs of nanorhombic shape with an average size of 10x20 nm (Figure 5.1(b)) were achieved when the OA:OM molar ratio was 3:7 and synthesis temperature was 150ºC. With increasing the

molar ratio of OA:OM to 6:4, the shape of NPs was changed to nanorod with a size of 10x20 nm (Figure 1(c)). Further increase of the molar ratio of OA:OM to 8:2 and treatment temperature to 180ºC, TiO_2 nanospheres were achieved with average diameter of 5-7 nm (Figure 5.1(a)). All the TiO_2 crystals were confirmed in anatase phase, in which XRD patterns exhibited strong diffraction peaks at 25°and 48° (Figure 5.2). From Figure 5.2, it was also shown that the diffraction pattern peak intensity of the TiO_2 increases in the order of nanorhombic, nanosphere and nanorod. These results suggested that the crystallinity of nanorod is higher than of nanosphere and of nanorhombic.

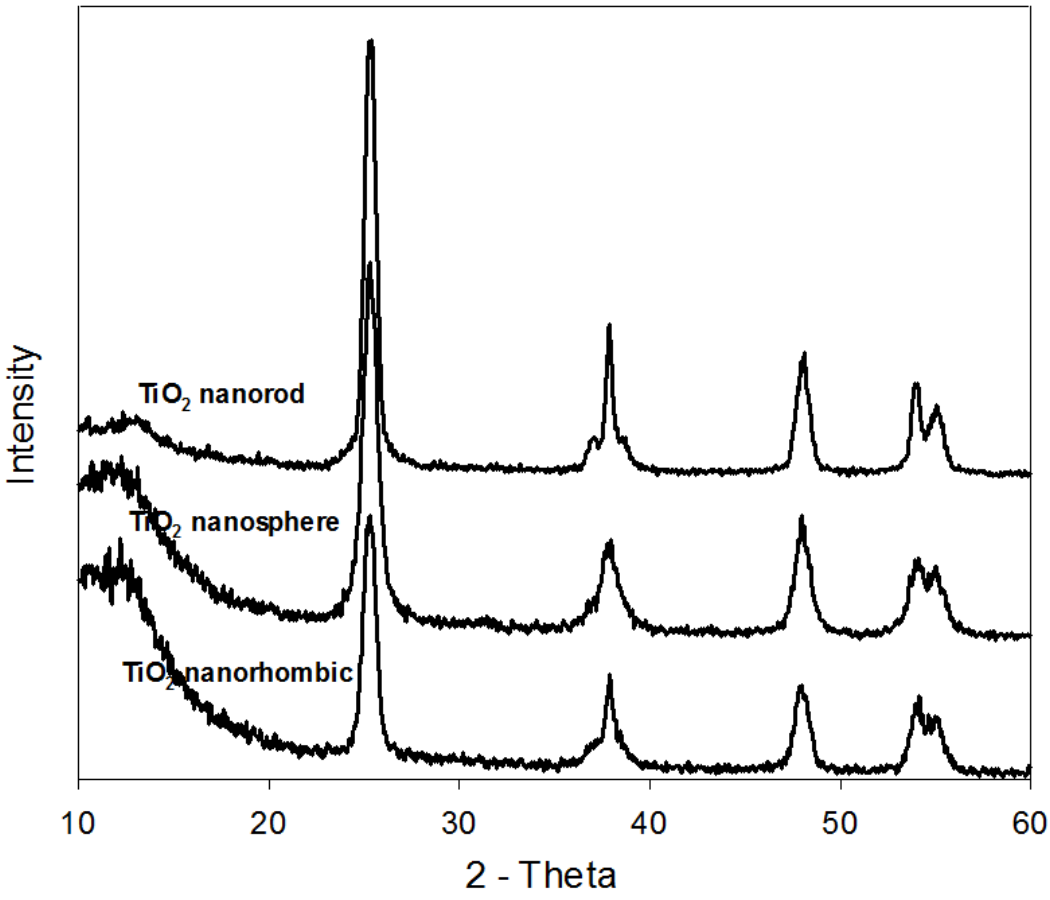

Figure 5.2. XRD of synthesized TiO_2 NPs with different shapes.

According to the fact that the shape of TiO_2 NPs was changed by changing the synthesis parameters, it could be assumed that the formation of TiO_2 NPs is indeed controlled by the ratio OA:OM, treatment temperature, and water/EtOH concentration. Two

consecutive processes took place: i) the hydrolysis of titanium precursors to create unstable hydroxyalkosides, and ii) the olation or oxolation of these unstable hydroxyalkosides to form Ti-O-Ti chains.[17] By controlling the rate of these two processes, the growing of TiO_2 NPs could be controlled, leading to different NPs shapes. As reported in literature,[18,19] the development of Ti-O-Ti chains is favored for low hydrolysis rates, low content of water and excess titanium precusors.[18] According to Livage et al.,[19] the amount of water presented in the reaction mostly contributed to the hydrolysis path as below:

$$Ti(OBu)_n + nH_2O \leftrightarrow Ti(OH)_n + n\text{BuOH} \quad \textbf{(5-1)}$$

Therefore, the hydrolysis rate is higher, the formation of Ti-OH is more favored for higher amount of water and the development of three-dimensional polymeric-like chains is insufficient, resulting in closely packed first-order particles.

In the synthesis system reported, when the heat treatment temperature is increased, water vapor generated from the mixture of water and EtOH is increased, hence greatly influences the creation of hydroxyalkosides. Together with water vapor, water excess in the 95% EtOH leads to the formation of prefered first-order particles (nanospheres), as shown in Figure 5.1(a), with average diameter of 5–7 nm. OA and OM surfactants also play important roles during the hydrolysis process as they generate water resulting from the acid-base pair catalyst. Moreover, these two surfactants are selective bindings to different faces of TiO_2, therefore they restrict TiO_2 NPs to grow in different directions. OA binds strongly to the TiO_2 {001} faces,[20] while OM binding is more favored on {101} faces.[21] When the molar ratio OA:OM is low (3:7 in our case), the adhesion of OM to the low surface energy {101} face leads to a more progressive TiO_2 growth along {001} to form nanorhombic TiO_2 NPs,[22] as shown in Figure 5.1(b). Increasing the molar ratio OA:OM to 6:4, the hydrolysis rate decreases and the growth along {001} is preserved leading to TiO_2 nanorod shape,[18] as shown in Figure 5.1(c).

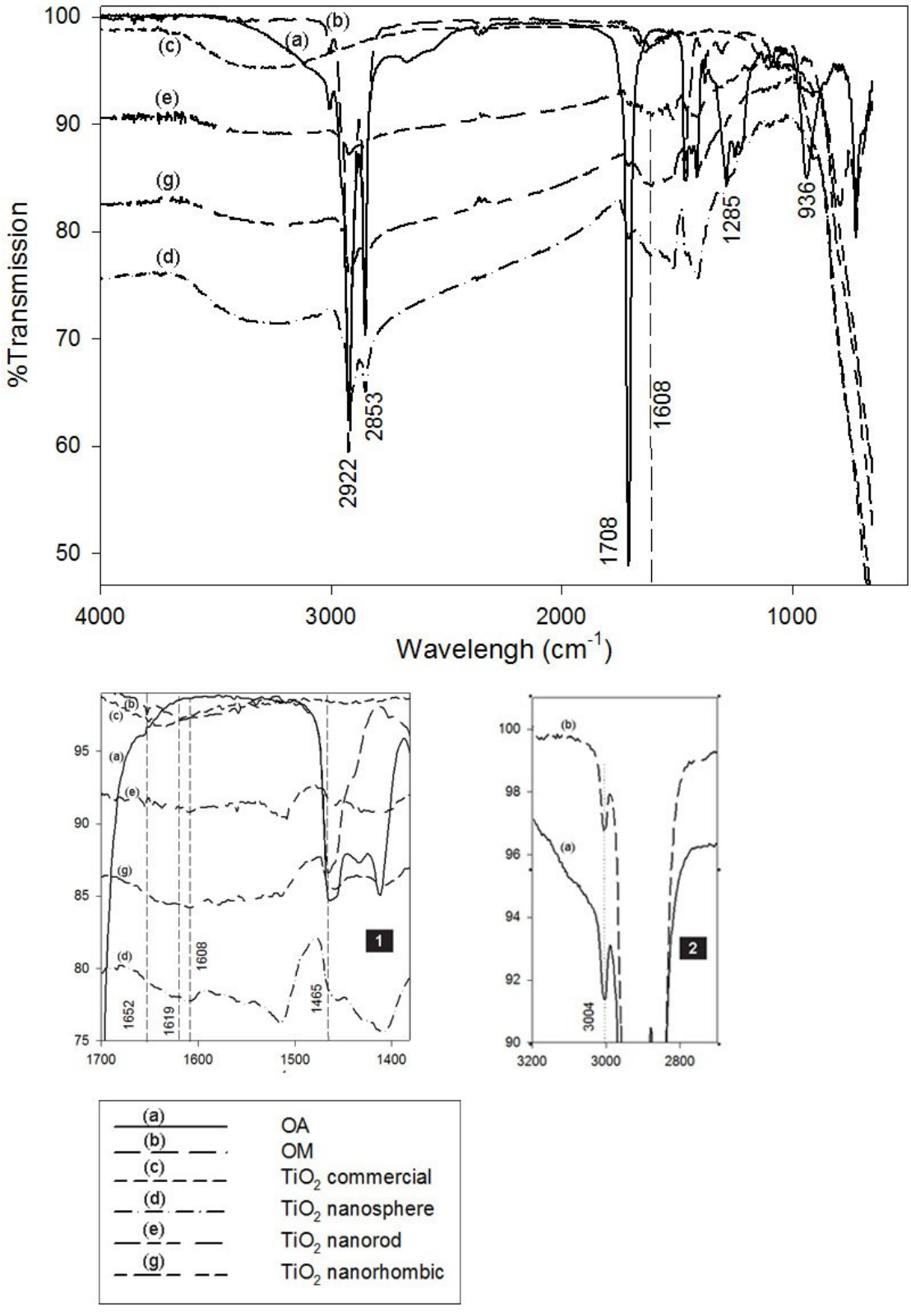

Figure 5.3. FTIR spectra of capped- TiO_2 NPs with different shapes; inset [1] in the region 1400-1700cm^{-1}; in set[2] in the region 2800-3200 cm^{-1}.

The FTIR spectra of the developed capped TiO_2 NPs with different shapes are shown in Figure 5.3 together with those of OA, OM and commercial TiO_2. OA and OM spectra show sharp vibrations bands at 2922 and 2853 cm^{-1}, which are attributed to asymmetric and symmetric C-H bonds in methylene groups (CH_2).[23] The vibrations at 1465 and 722 cm^{-1} are due to the characteristic of $-(CH_2)_n-$ chains with $n > 3$;[24] the small peaks at 3004 cm^{-1} correspond to the stretching of =C-H bond. The peaks at 1708 and 1285 cm^{-1} in the spectrum of OA are assigned to C=O and C-O stretch, respectively. Those appearing at 1463 and 936 cm^{-1} are respectively due to in-plane and out-of plane O-H. In the spectrum of OM, the vibrations at 1652 and 1619 cm^{-1} correspond to the combined motion of NH_2 scissoring and N-H bending. The peak at absorbed at 1041 cm^{-1} is a characteristic peak of the C-N stretch. Compared to the spectrum of commercial TiO_2, the presence of capping ligand on the surface of the synthesized capped TiO_2 NPs is identified by the peaks at 3004, 2922, 2853, and 1465 cm^{-1}. However, the intensities of the absorption bands corresponding to those of OA and OM are small. This is due to the fact that only small amounts of OA and OM surfactants are expected to be left on the surface of TiO_2 NPs. The vibration at 1708 cm^{-1}, which is the characteristic band of carbonyl in carboxyl acid, doesn't appear in the spectra of capped TiO_2 NPs. However, a new peak appears at 1608 cm^{-1}; this indicates the existence of carboxylic acid salt on the surface of capped TiO_2 NPs. This carboxylic acid salt is the result of the reaction between OA surfactant and TiO_2 NPs during the solvothermal process. Furthermore, the weak absorbance peak appearing at 1041 cm^{-1} on the three spectra of capped TiO_2 NPs (which corresponds to the peak of C-N bonds in the amine groups) proves the existence of oleyl amine on the surface of capped TiO_2 NPs.

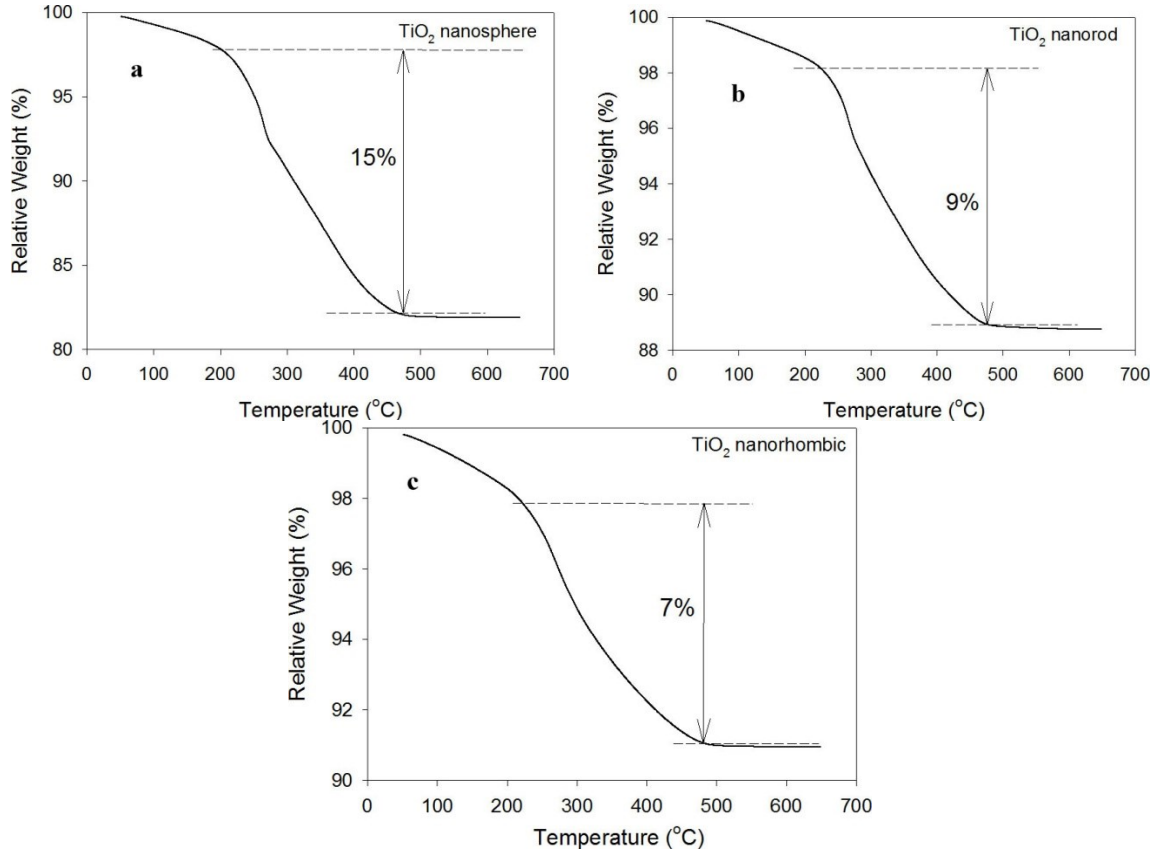

Figure 5.4. TGA curves of TiO_2 NPs characterized at a heating rate of 10 ºC/min under O_2 atmosphere.

Thermal characterisation of synthesized capped TiO_2 NPs of different shapes are summarized in TGA plots of Figure 5.4, obtained at a heating rate of 10ºC/min under O_2 atmosphere. All the three curves corresponding to nanosphere, nanorod, and nanorhombic TiO_2 shapes show an initial weight loss starting from 50ºC. This is attributed to the water absorbed on the surface of TiO_2 NPs. obviously, the most significant weight loss occured between 200 and 480ºC corresponds to OA and OM surfactants. For higher temperatures (>480ºC), the three thermogravimetric curves show very small wheigh loss, which could be attributed to the decomposition of residual product traces that forms a sheath over the TiO_2 NPs.[25]

TGA characterization puts in evidence the presence of OA and OM surfactants on the surface of the three capped TiO_2 NPs (nanosphere, nanorod and nanorhombic) at weight ratios of about 15, 9 and 7 wt%, respectively. The high percentage of the organic part at the

surface of TiO_2 NPs contributes to the high solubility of these NPs in common organic solvents, such as toluene and chloroform. However, this could affect the charge transfer at the interface of NPs.[24]

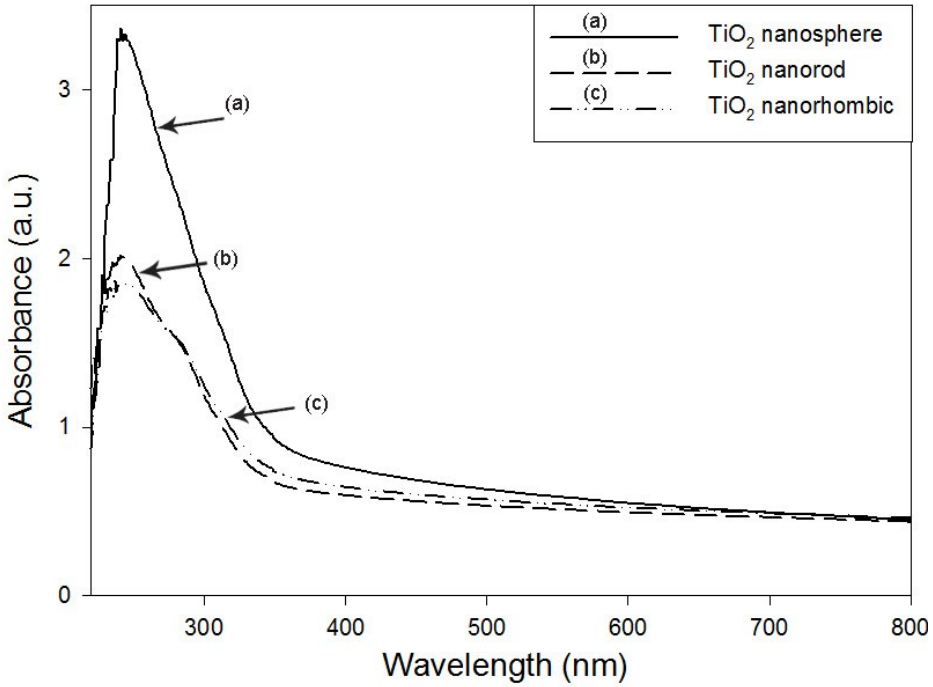

Figure 5.5. UV-vis absorption spectra of the three synthesized TiO_2 NPs of different shapes in $CHCl_3$ solvent.

The optical properties of the synthesized capped TiO_2 NPs with different shapes, disloved in Cloroform solvant, were characterized by UV-vis spectrometer. The corresponding spectra are shown in Figure 5.5. Since TiO_2 is an indirect band gap semiconductor with a large bandgap, E_g ($E_g \approx 3.2eV$ for anatase), the optical bandgap E_g can be determined from the absorption coefficient, α, which depends on the wavelength, λ. When scattering effects are neglected, the absorption coefficient near the absorption edge for indirect inter-band transition is given by the following relation:[26]

$$\alpha = B_i(h\nu - E_g)^2 / h\nu \quad \textbf{(5-2)}$$

where B_i is the absorption constant for indirect transition, h is the Plank's constant, and ν is the frequency of radiation (Hz).

From the UV-Vis spectra of three TiO_2 NPs with different shapes, the value of α and related photon energy could be obtained. By plotting the graph of $(\alpha h\nu)^{1/2}$ versus photon energy $E(=h\nu)$, the intersection of the tangent to the curve and the X-axis gives the bandgap of the NPs, as shown in Figure 5.6. Therefore, band gap energies for the three shapes of capped TiO_2 NPs were: 2.88 eV for TiO_2 nanospheres, 2.66 eV for TiO_2 nanorods and 2.48 eV for TiO_2 nanorhombic.

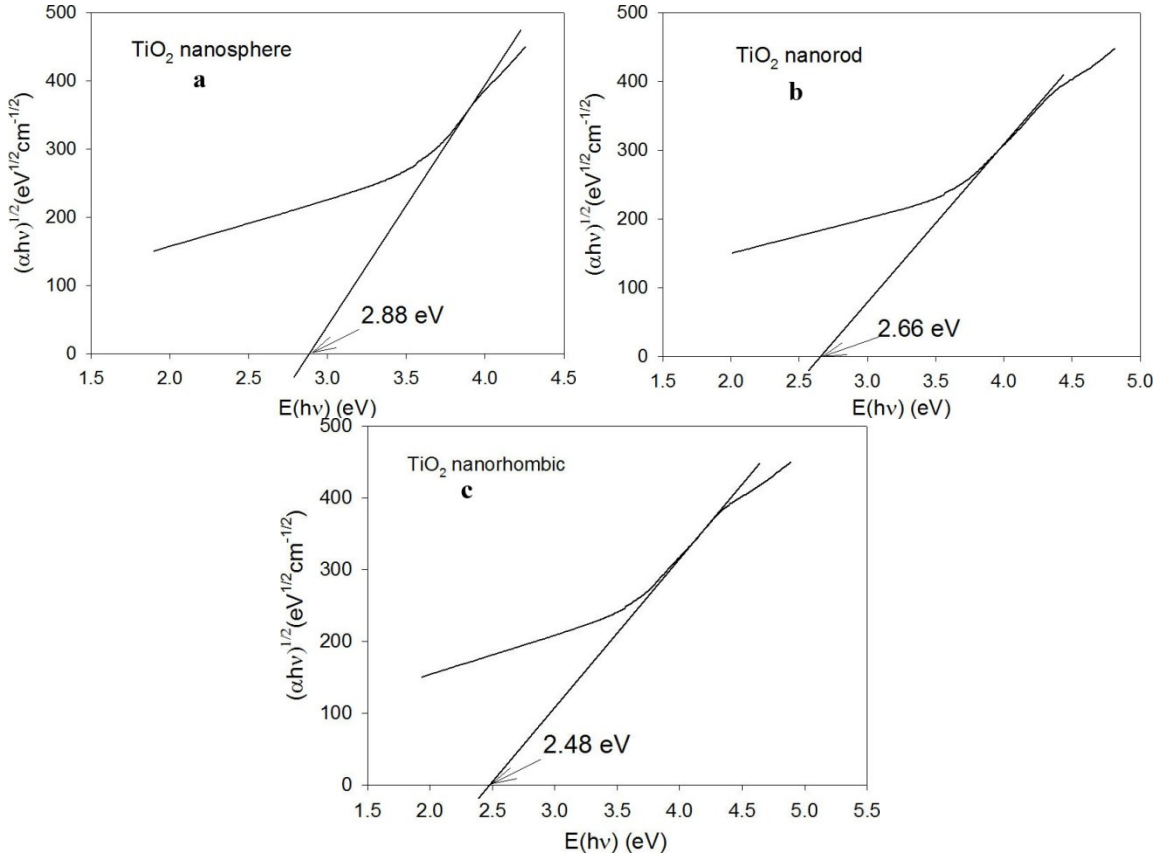

Figure 5.6. Band gaps of the three synthesized TiO_2 NPs determined from the plot of versus photon energy: (a) nanosphere, (b) nanorod, and (c) nanorhombic.

It is well known that in semiconductors, when a photon is absorbed, an electron-hole pair or an exciton is formed. The normal size of an exciton in bulk crystal (defined a critical quantum measurement or exciton Bohr radius) gives an approximate dimension for the onset of quantum confinement effects.[27] When electrons and holes are being squeezed into a dimension that approaches the critical quantum measurement, they lead to some change in electronic state symmetries, in the state energy, in the overall shape and symmetry of the wave function, in the polarization, as well as in localization. All of these changes lead to an increase of the effective bandgap.[28] Hence, any difference in shape of nanocrystals results in a difference in the magnitude of the quantum confinement and effective bandgap. Results shown in Figure 5.6 confirm again the relationship between bandgap energy and the shape of TiO_2 NPs.

5.3.2. Development and characterization of MEH-PPV/TiO_2 nanocomposite films

The dispersion of TiO_2 NPs in MEH-PPV/ TiO_2 nanocomposite were characterized by TEM (Figure 5.7). Those results show well dispersed-TiO_2 NPs on the films. However, the dispersion of TiO_2 nanospheres and nanorods seem to be better than that of TiO_2 nanorhombics. This could be explained by the different amount of surfactants capped on TiO_2 NPs surfaces, which leads to the different solubility of different TiO_2 NPs in chloroform solvent.

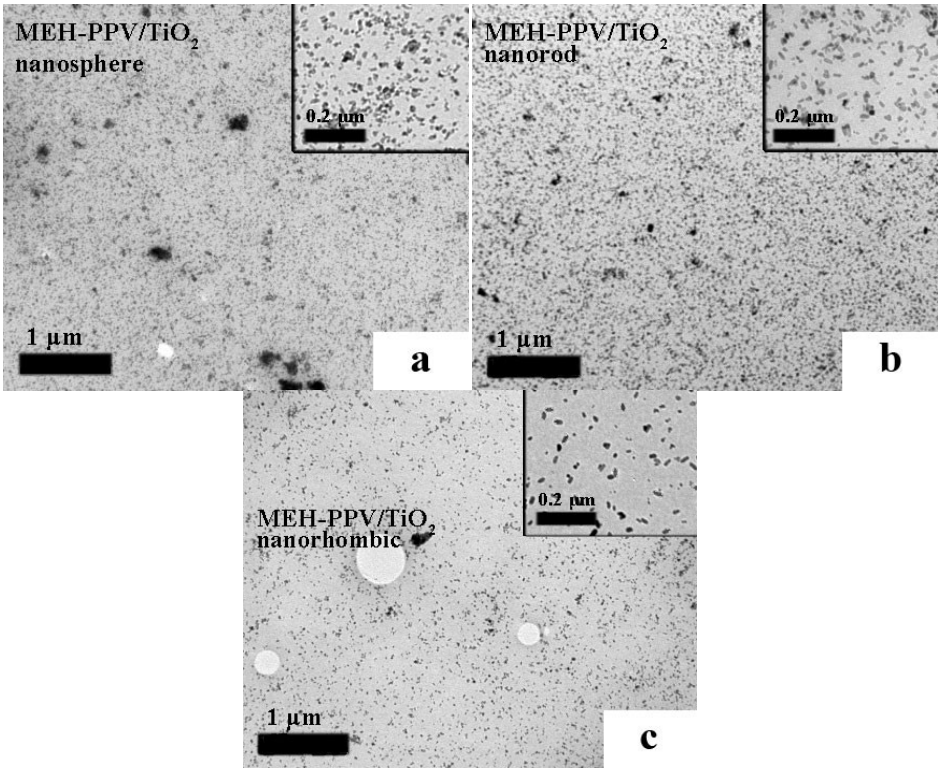

Figure 5.7. TEM of composite of MEH-PPV and synthesized TiO_2 NPs with different shapes: (a) nanosphere, (b) nanorhombic, and (c) nanorod

TGA characterization of pure MEH-PPV and MEH-PPV/TiO_2 nanocomposites were done to observe the stability of materials. Figure 5.8(a) shows typical TGA curves of normalized mass and derivative thermogravimetry (DTG) data of the derivative of mass as functions of temperature for MEH-PPV at a heating rate of 10 $^oC\ min^{-1}$ in air environment. In air, the first stage of degradation reaction begins around 280 ^oC and stops around 390 ^oC, with the maximum rate at 333 ^oC. The second and third stages of the decompositions appear between 390 and 452 ^oC with a maximum rate of mass loss around 417 ^oC, and between 452 and 560 ^oC with a maximum rate of mass loss around 506 ^oC, respectively.

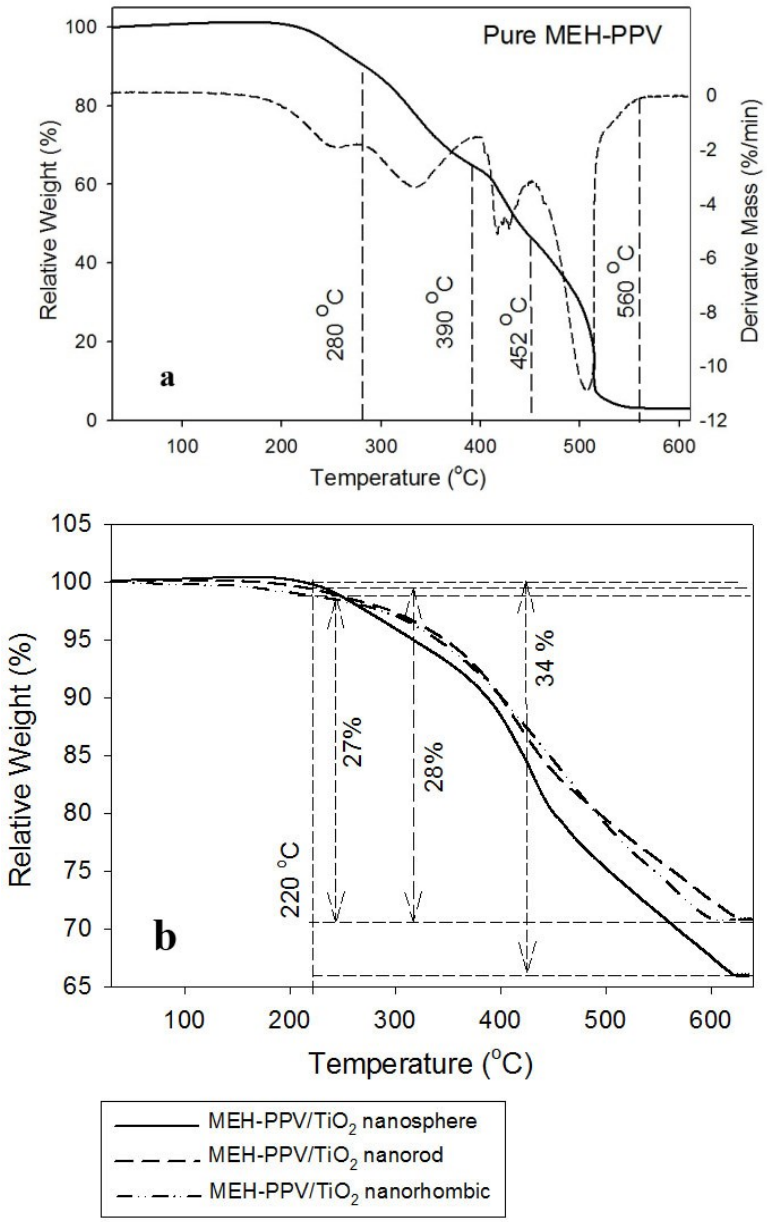

Figure 5.8. TGA curves of (a) pure MEH-PPV (b) MEH-PPV/TiO_2 nanocomposites characterized at a heating rate of 10 ºC/min under air atmosphere.

Figure 5.8(b) are the TGA characterization of MEH-PPV/TiO_2 NPs composites. As the composite of MEH-PPV and TiO_2 NPs were prepared using blending solution, in which there is no chemical bonding building up between two materials. The TGA characterization of MEH-PPV/TiO_2 NPs composite with 20 wt% MEH-PPV shows the curves which are expected to be the sum of both TGA curve of pure MEH-PPV and TiO_2 NPs. The weight

loss of three composites (MEH-PPV/-nanosphere, -nanorod, -nanorhombic) are 34, 28, 27 %, respectively. The weight loss of composite is in agreement with the assumption, where the total weight loss of composite is equal to the weight loss of 20 wt% MEH-PPV in the composite, and weight loss of TiO_2 NPs.

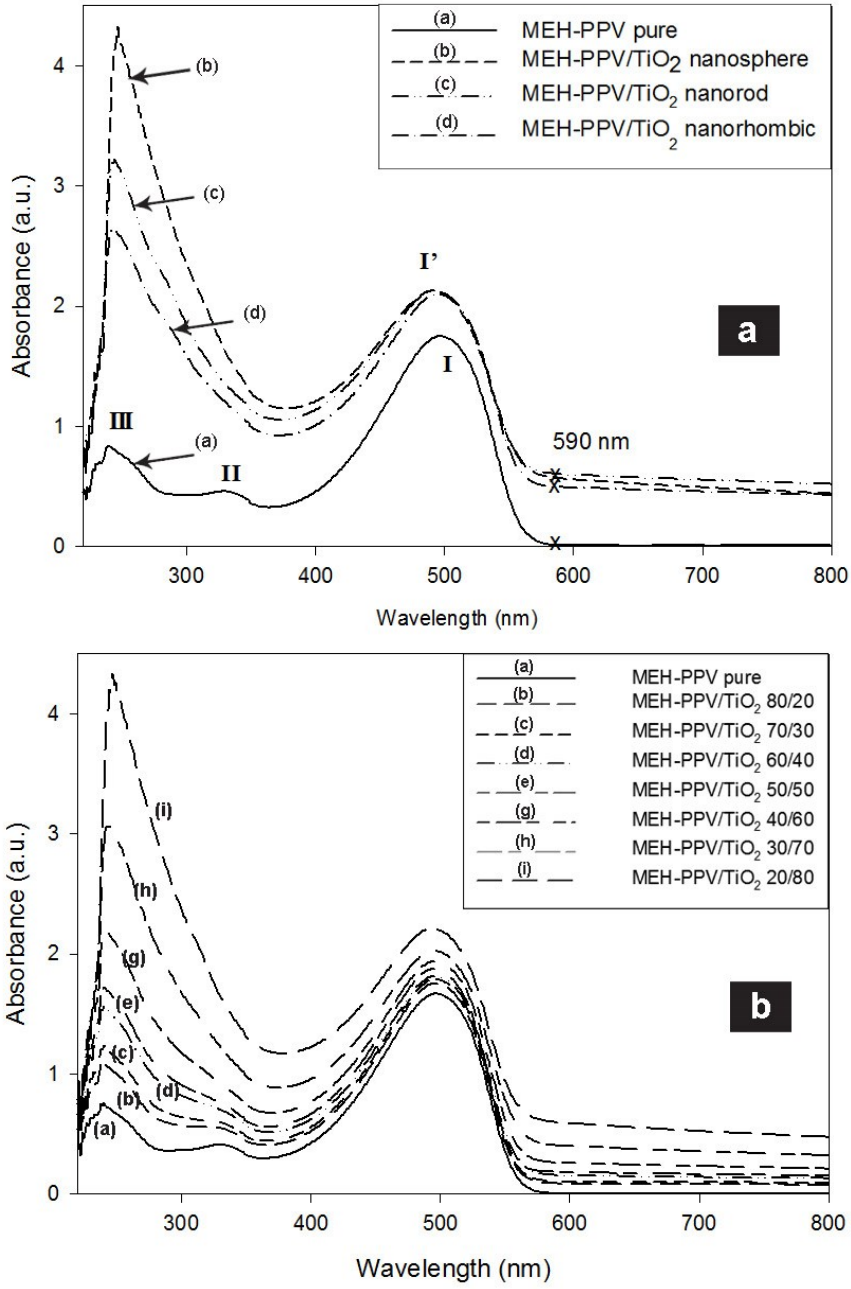

Figure 5.9. UV-vis absorption spectra of MEH-PPV/TiO_2 nanocomposites: (a) different TiO_2 shapes, and (b) TiO_2 nanospheres of different concentrations.

Figure 5.9(a) shows the UV-vis absorption spectra for pure MEH-PPV and three MEH-PPV/TiO_2 nanocomposites developed with the three different shapes of capped TiO_2 NPs. The weight composition of these three nanocomposites was maintained constant (weight ratio MEH-PPV/TiO_2 = 20/80). As shown in Figure 5.9(a), the three spectra of the nanocomposites show a sharp onset at absorption near 590 nm (2.1 eV) and two evident peaks corresponding to MEH-PPV matrix and capped TiO_2 NPs. The MEH-PPV spectrum also shows a sharp onset near 590 nm (2.1 eV); however, it shows three absorption peaks at ~500, 330 and 240 nm in the region between 220 and 800 nm, which are expected for PPV-derivatives.[29] The first maximum peak I near 500nm is attributed to the $\pi - \pi^*$ transition of MEH-PPV conjugated polymer.[30] However, when TiO_2 is added, this peak position is blue-shifted to peak I' at 496 nm (2.5 eV). The second small peak II at 330 nm (3.76 eV) is not observed for the three nanocomposites due to the resonance of wavelength between MEH-PPV and added TiO_2 NPs. The intensity of third peak III at 240 nm (5.12 eV) was observed to increase and red-shifted (~ 0.1 eV) with the addition of TiO_2. Moreover, no additional absorption peaks and no major shift of wavelength in the visible region (390 - 750 nm) were observed for the three MEH-PPV/TiO_2 nanocomposites. This indicates that there is no evidence of ground-state charge-transfer between the MEH-PPV matrix and TiO_2 NPs and consequently, there is no chemical bonding between MEH-PPV and TiO_2 NPs. By mixing MEH-PPV and capped TiO_2 NPs, the optical absorption of the MEH-PPV/TiO_2 composite increases due to the fact that TiO_2 NPs also contribute to light harvesting, particularly in the visible region. The increase in optical absorption can be attributed to scattering caused by TiO_2 NPs in the MEH-PPV matrix.[9] As a result, the optical absorption of MEH-PPV/TiO_2 nanocomposites increases with increasing TiO_2 concentration, as shown in Figure 5.9(b) for TiO_2 nanospheres.

Figure 5.10 shows FTIR spectra for pure MEH-PPV and the three MEH-PPV/TiO_2 (20/80) nanocomposites developed using the three TiO_2 shapes. All the four spectra show the same IR absorption peaks. In a previous study,[31] the authors reported a C-O-Ti absorption band at 1265 cm^{-1}; however, this band is not observed in our study, which confirms that there is no chemical bonding between the MEH-PPV matrix and the dispersed TiO_2 NPs.

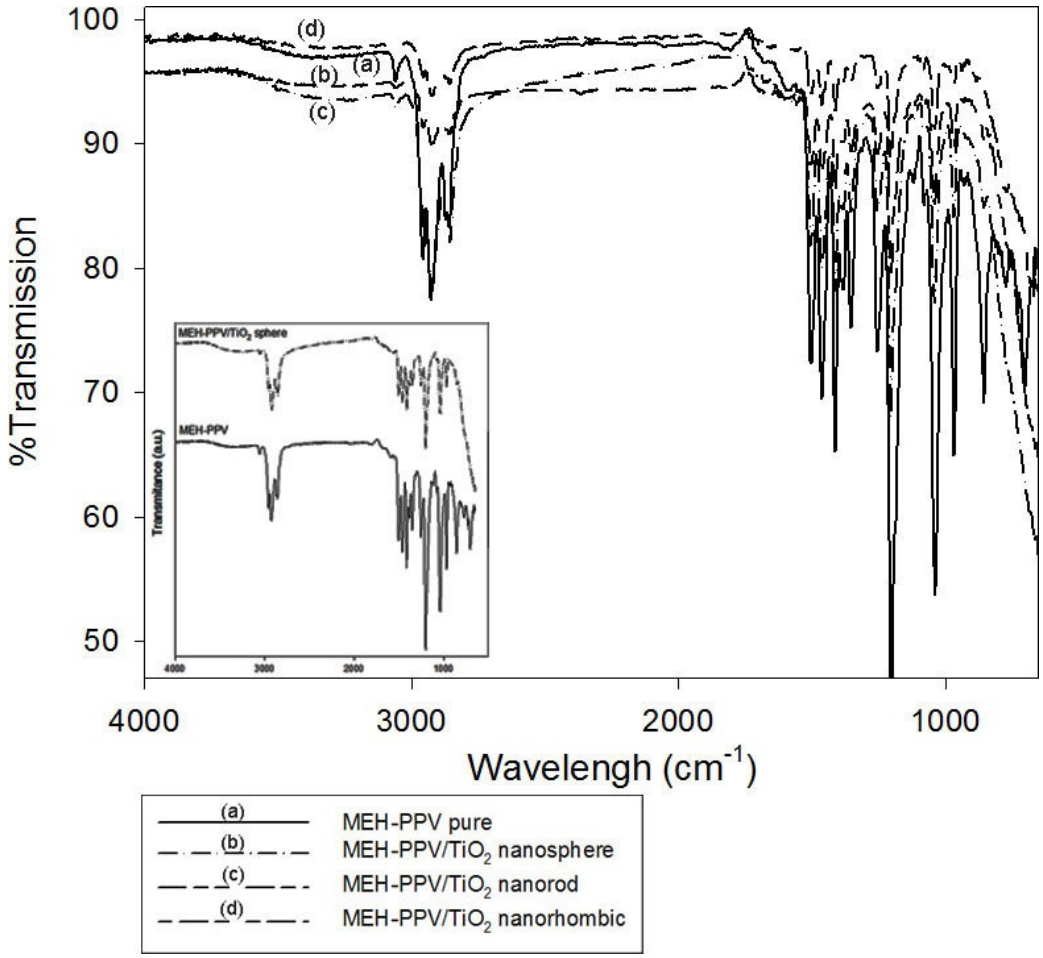

Figure 5.10. FTIR of MEH-PPV and MEH-PPV/TiO_2 nanocomposites. Bottom inset: FTIR spectra of MEH-PPV and MEH-PPV/TiO_2 nanocomposites using TiO_2 nanospheres.

Figure 5.11 shows the photoluminescence (PL) emission spectra for pure MEH-PPV and MEH-PPV/TiO_2 nanocomposites at room temperature under excitation at a wavelength of 495nm. PL emission refers to the spontaneous emission of light by a material under optical excitation. PL quenching was used as a powerful measure of the efficiency of charge transfer in donor-acceptor blend films.[32] The decrease in PL intensity indicates a better PL quenching. It also indicates a decrease in light emission of the material or a better charge transfer within the materials. For all the MEH-PPV/TiO_2 nanocomposites, the PL spectra show peaks at 560 and 600 nm corresponding to those of MEH-PPV. Even though the PL emission of pure MEH-PPV is not affected by the addition capped TiO_2 NPs, there is a significant difference in the quenching of PL emission intensity with respect to the

shape of TiO_2 NPs (Figure 5.11(a)) and also with respect to the concentration of TiO_2 NPs (Figure 5.11(b)).

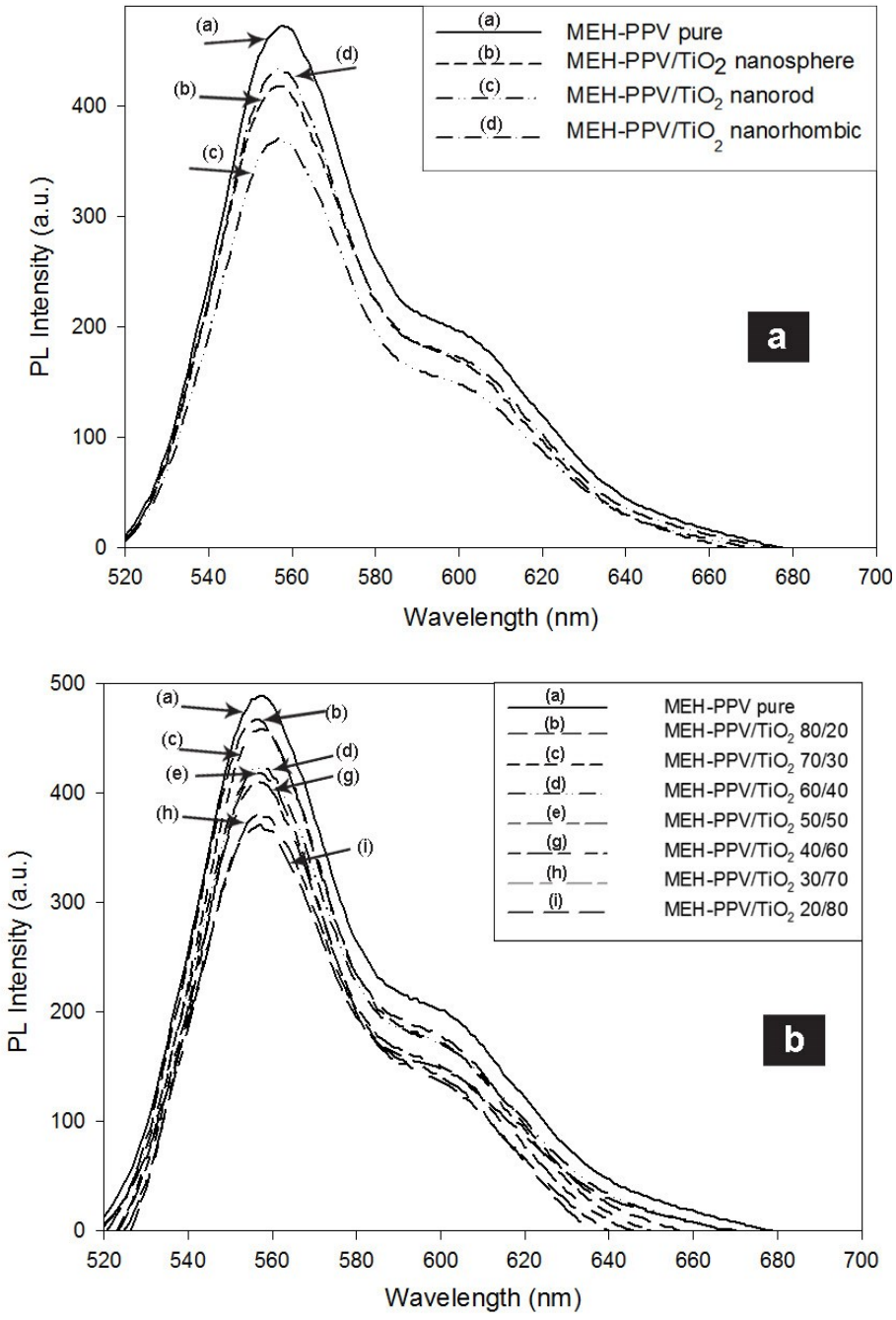

Figure 5.11. Photoluminescence (PL) emission of MEH-PPV/ TiO_2 nanocomposites: (a) different TiO_2 shapes, and (b) TiO_2 nanorods of different concentrations.

It is important to mention that PL quenching due to the presence of TiO_2 NPs can be attributed to either energy or charge transfer from the MEH-PPV matrix to the inorganic dispersed TiO_2 NPs. In general, a better PL quenching is an indication of a better dispersion of TiO_2 NPs. It is evident from Figure 11(a) that the quenching of fluorescence is significantly higher for nanorod than nanosphere capped TiO_2 NPs. This can be explained by the higher surface-to-volume ratio, and also by the higher delocalization of carriers in nanorods compared to nanospheres. This helps to increase the probability of charge transfer at polymer-NPs interface, and also helps to prevent the back recombination of holes in MEH-PPV matrix and electrons in TiO_2 NPs.[33] However, results show that the emission quenching for nanorhombic TiO_2 NPs was lower than that obtained for TiO_2 nanospheres. This can be due to the fact that nanorhombic TiO_2 NPs have bigger size than TiO_2 nanospheres, which affects their distribution in the MEH-PPV matrix. The interface between these nanorhombic TiO_2 NPs and the MEH-PPV matrix is then decreased and as a consequence, the probability of charge transfer at the interface is also decreased. Now, let us discuss the effect of OA and OM surfactants capped on the surface of TiO_2 NPs. As mentioned before, nanorhombic and nanorod TiO_2 NPs have similar sizes and are both expected to have higher surface-to-volume ratio and higher delocalization than TiO_2 nanospheres. The only difference is the amount of capped OA and OM surfactants, which, as presented in section 3.1 were around 9 wt% for nanorod TiO_2 NPs and around 7 wt% for nanorhombic TiO_2 NPs. Surfactants have been reported to form a barrier that prevents charge transfer at the interface with the polymer matrix but helps to improve the contact area between NPs and polymer chains, which increases the charge transfer at the surface of materials.[34] Presently, there is no clear explanation about which factor between the shape of NPs and the amount of surfactants on the surface of these NPs dominates the charge transfer at the interface of the polymer matrix and the dispersed NPs. However, comparison of PL results presented in this study for MEH-PPV/TiO_2 nanocomposites developed with nanorod and nanorhombic TiO_2 NPs shows that the impact of ON and OM surfactants seems to be greater than that of TiO_2 particle size.

For TiO_2 nanorod shape, Figure 5.11(b) shows PL intensity for MEH-PPV/TiO_2 nanocomposites of various TiO_2 concentrations. For small TiO_2 concentrations (up to 40 wt%), PL intensity shows a small decrease. However, for higher TiO_2 concentrations, PL

quenching increases with increasing TiO_2 concentration. This increase reaches around 20% when TiO_2 NPs concentration is around 80wt%.

5.4. Conclusions

Simple solvothermal routine in autoclave was successfully used to synthesize TiO_2 NPs of different shapes (nanospheres, nanorods and nanorhombics) using OA and OM as capping agents. The presence of OA and OM on the surface of the synthesized TiO_2 NPs was confirmed by FTIR characterization and their quantitative characterization was done using TGA under O_2 atmosphere. It was found that the shape of NPs and the amount of OA and OM surfactants capped on their surface have an effect on their energy bandgap and also on the dispersion quality of MEH-PPV/TiO_2 nanocomposites. Even though there was no evidence of chemical bonding between MEH-PPV matrix and TiO_2 dispersed NPs, MEH-PPV/TiO_2 nanocomposites showed very promising results for light absorption and coupled electron/hole transport, which are two main characteristics for photovoltaic materials. Work is presently focused on the optimization of TiO_2 dispersion in the MEH-PPV matrix using the three developed NPs shapes.

Acknowledgements

The authors would like to thank the Natural Sciences and Engineering Research Council of Canada (NSERC) for financial support of this work.

5.5. Reference

(1) Chapin, D. M.; Fuller, C. S.; Pearson, G. L. *J. Appl. Phys.* **1954**, *25*, 676.

(2) Brabec, C. J.; Sariciftci, N. S.; Hummelen, J. C. *Adv. Funct. Mater.* **2001**, *11*, 15–26.

(3) Mihailetchi, V. D.; Koster, L. J. a.; Blom, P. W. M. *Appl. Phys. Lett.* **2004**, *85*, 970.

(4) Kim, Y.; Choulis, S. a.; Nelson, J.; Bradley, D. D. C.; Cook, S.; Durrant, J. R. *Appl. Phys. Lett.* **2005**, *86*, 063502.

(5) Kang, Y.; Kim, D. *Sol. Energy Mater. Sol. Cells* **2006**, *90*, 166–174.

(6) Ram, M. K.; Sarkar, N.; Bertoncello, P.; Sarkar, A.; Narizzano, R.; Nicolini, C. *Synth. Met.* **2001**, *122*, 369–378.

(7) Wu, M.-C.; Lo, H.-H.; Liao, H.-C.; Chen, S.; Lin, Y.-Y.; Yen, W.-C.; Zeng, T.-W.; Chen, Y.-F.; Chen, C.-W.; Su, W.-F. *Sol. Energy Mater. Sol. Cells* **2009**, *93*, 869–873.

(8) Al-Ibrahim, M.; Roth, H.-K.; Zhokhavets, U.; Gobsch, G.; Sensfuss, S. *Sol. Energy Mater. Sol. Cells* **2004**, *85*, 13–20.

(9) Verma, D.; Ranga Rao, A.; Dutta, V. *Sol. Energy Mater. Sol. Cells* **2009**, *93*, 1482–1487.

(10) Huynh, W. U.; Dittmer, J. J.; Alivisatos, a P. *Science* **2002**, *295*, 2425–2427.

(11) Wang, L.; Liu, Y.; Jiang, X.; Qin, D.; Cao, Y. *J. Phys. Chem. C* **2007**, *111*, 9538–9542.

(12) Roberson, L. B.; Poggi, M. A.; Kowalik, J.; Smestad, G. P.; Bottomley, L. A.; Tolbert, L. M. *Coord. Chem. Rev.* **2004**, *248*, 1491–1499.

(13) Ginger, D. S.; Greenham, N. C. *Synth. Met.* **2001**, *124*, 117–120.

(14) Salafsky, J. *Phys. Rev. B* **1999**, *59*, 10885–10894.

(15) Nelson, J. *Curr. Opin. Solid State Mater. Sci.* **2002**, *6*, 87–95.

(16) Dinh, C.; Nguyen, T.; Kleitz, F.; Do, T. *ACS Nano* **2009**, *3*, 3737–3743.

(17) Bessekhouad, Y.; Robert, D.; Weber, J. V. *J. Photochem. Photobiol. A Chem.* **2003**, *157*, 47–53.

(18) Li, X.-L.; Peng, Q.; Yi, J.-X.; Wang, X.; Li, Y. *Chemistry* **2006**, *12*, 2383–2391.

(19) Livage, J.; Henry, M.; Sanchez, C. *Prog. Solid St. Chem.* **1988**, *18*, 259–341.

(20) Joo, J.; Kwon, S. G.; Yu, T.; Cho, M.; Lee, J.; Yoon, J.; Hyeon, T. *J. Phys. Chem. B* **2005**, *109*, 15297–15302.

(21) Jun, Y.-W.; Casula, M. F.; Sim, J.-H.; Kim, S. Y.; Cheon, J.; Alivisatos, A. P. *J. Am. Chem. Soc.* **2003**, *125*, 15981–15985.

(22) Wu, B.; Guo, C.; Zheng, N.; Xie, Z.; Stucky, G. D. *J. Am. Chem. Soc.* **2008**, *130*, 17563–17567.

(23) Limaye, M. V; Singh, S. B.; Date, S. K.; Kothari, D.; Reddy, V. R.; Gupta, A.; Sathe, V.; Choudhary, R. J.; Kulkarni, S. K. *J. Phys. Chem. B* **2009**, *113*, 9070–9076.

(24) Chen, S.; Liu, W. *Mater. Chem. Phys.* **2006**, *98*, 183–189.

(25) Tzitzios, V.; Niarchos, D.; Margariti, G.; Fidler, J.; Petridis, D. *Nanotechnology* **2005**, *16*, 287–291.

(26) Serpone, N.; Lawless, D.; Khairutdinov, R. *J. Phys. Chem.* **1995**, *99*, 16646–16654.

(27) Buhro, W. E.; Colvin, V. L. *Nat. Mater.* **2003**, *2*, 138–139.

(28) Li, J.; Wang, L.-W. *Nano Lett.* **2003**, *3*, 1357–1363.

(29) Miller, E.; Yoshida, D.; Yang, C.; Heeger, A. *Phys. Rev. B* **1999**, *59*, 4661–4664.

(30) Kim, S.-S.; Jo, J.; Chun, C.; Hong, J.; Kim, D. *J. Photochem. Photobiol. A Chem.* **2007**, *188*, 364–370.

(31) Su, B.; Ma, Z.; Min, S.; She, S.; Wang, Z. *Mater. Sci. Eng. A* **2007**, *458*, 44–47.

(32) Greenham, N.; Peng, X.; Alivisatos, A. *Phys. Rev. B* **1996**, *54*, 17628–17637.

(33) Petrella, A.; Tamborra, M.; Curri, M. L.; Cosma, P.; Striccoli, M.; Cozzoli, P. D.; Agostiano, A. *J. Phys. Chem. B* **2005**, *109*, 1554–1562.

(34) Liu, J.; Wang, W.; Yu, H.; Wu, Z.; Peng, J.; Cao, Y. *Sol. Energy Mater. Sol. Cells* **2008**, *92*, 1403–1409.